

Thermoelectric properties of the Corbino disk in graphene

Adam Rycerz*,¹ Katarzyna Rycerz,² and Piotr Witkowski¹

¹*Institute for Theoretical Physics, Jagiellonian University, Lojasiewicza 11, PL-30348 Kraków, Poland*

²*Institute of Computer Science, AGH University of Science and Technology, al. Mickiewicza 30, PL-30059 Kraków, Poland*

(Dated: June 2, 2023)

Thermopower and the Lorentz number for an edge-free (Corbino) graphene disk in the quantum Hall regime is calculated within the Landauer-Büttiker formalism. By varying the electrochemical potential, we find that amplitude of the Seebeck coefficient follows a modified Goldsmid-Sharp relation, with the energy gap defined by the interval between the zero and the first Landau levels in bulk graphene. An analogous relation for the Lorentz number is also determined. Thus, these thermoelectric properties are solely defined by the magnetic field, the temperature, the Fermi velocity in graphene, and fundamental constants including the electron charge, the Planck and Boltzmann constants, being independent on geometric dimensions of the system. This suggests that the Corbino disk in graphene may operate as a thermoelectric thermometer, allowing to measure small temperature differences between two reservoirs, if the mean temperature and the magnetic field are known.

I. INTRODUCTION

Almost twenty years after the discovery of graphene [1–3], a two-dimensional form of carbon hosting ultrarelativistic effective quasiparticles [2, 3], which forced researchers to re-examine numerous effects previously known from mesoscopic physics [4–10], it seems that the development of quantum Hall resistance standards [11–13] can be considered as the most important application to emerge from this field of research. Although the Hall bar setup is most commonly used (also in the study of artificial graphene analogues [14–16]), the edge-free Corbino geometry is often considered when discussing fundamental aspects of graphene [6, 17–25]. In such a geometry, magnetotransport at high fields is unaffected by edge states, allowing one to probe the bulk transport properties [22–24]. Recently, sharp resonances in the longitudinal conductivity, associated with Landau levels, have been observed in graphene disks on hexagonal boron nitride [22].

In addition to conductivity measurements, thermoelectric phenomena including Seebeck and Nerst effects in graphene [26–35] and other two-dimensional systems [36–39] have been studied thoroughly, providing valuable insights into the details of the electronic structure of these materials. In particular, for systems with a wide bandgap E_g , the maximum absolute value of the Seebeck coefficient can be approximated by a Goldsmid-Sharp value [40, 41]

$$|S|_{\max} \approx \frac{E_g}{2eT}, \quad \text{for } E_g \gg k_B T, \quad (1)$$

with the absolute temperature T , the electron charge $-e$, and the Boltzmann constant k_B . (For more accurate approximations, see Ref. [31].)

The thermoelectric properties of graphene disks at zero (or low) magnetic fields have also been considered [42, 43]. In the quantum Hall regime, thermoelectricity has been studied for GaAs/AlGaAs based Corbino disks which host a two-dimensional gas of non-relativistic electrons [44–47]. However, analogous studies for graphene disks are missing so far.

In this paper, we present numerical results on the Seebeck coefficient and the Lorentz number (quantifying the ratio of thermal to electrical conductivity) for the ballistic disk in graphene (see Fig. 1). The results show that although the deviations from Eq. (1) are noticeable, the thermopower amplitude (determined by varying the doping at fixed temperature T and field B) can still be truncated by a closed-form function of the quantity $\Delta E_{\max}/(2eT)$, where $\Delta E_{\max} \propto \sqrt{B}$ is the maximum interval between Landau levels (LLs), playing a role of the transport gap. A similar conclusion applies to the maximum Lorentz number. Unusual sequence of LLs in graphene leads to relatively high thermoelectric response is expected for micrometer-size disks at moderate fields $B < 0.5$ T and few Kelvin temperatures. The effect of smooth potential profiles is also discussed, introducing the electron-hole asymmetry of the transport properties [48, 49].

The remaining parts of the paper are organized as follows. In Sec. II we present details of our numerical approach, which can be applied either in the idealized case where the electrostatic potential energy is a piecewise-constant function of the distance from the disk center, or in the more general case of smooth potentials. Our numerical results for both cases are presented in Sec. III. The conclusions are given in Sec. IV.

II. MODEL AND METHODS

A. Scattering of Dirac fermions

Our analysis starts with the wave equation for massless Dirac fermions in graphene at energy E and uniform magnetic field B , which can be written as (for the K valley)

$$[v_F (\mathbf{p} + e\mathbf{A}) \cdot \boldsymbol{\sigma} + V(r)] \Psi = E\Psi, \quad (2)$$

where $v_F = \sqrt{3}t_0a/(2\hbar) \approx 10^6$ m/s is the energy-independent Fermi velocity in graphene (with $t_0 = 2.7$ eV the nearest-neighbor hopping integral and $a = 0.246$ nm the lattice parameter), $\mathbf{p} = (p_x, p_y)$ is the in-plane momentum operator with $p_j = -i\hbar\partial_j$, we choose the symmetric gauge $\mathbf{A} = \frac{B}{2}(-y, x)$, and $\boldsymbol{\sigma} = (\sigma_x, \sigma_y)$, where σ_j are the Pauli matrices. The electrostatic potential energy $V(r)$ depends only

*Corresponding author; e-mail: rycerz@th.if.uj.edu.pl.

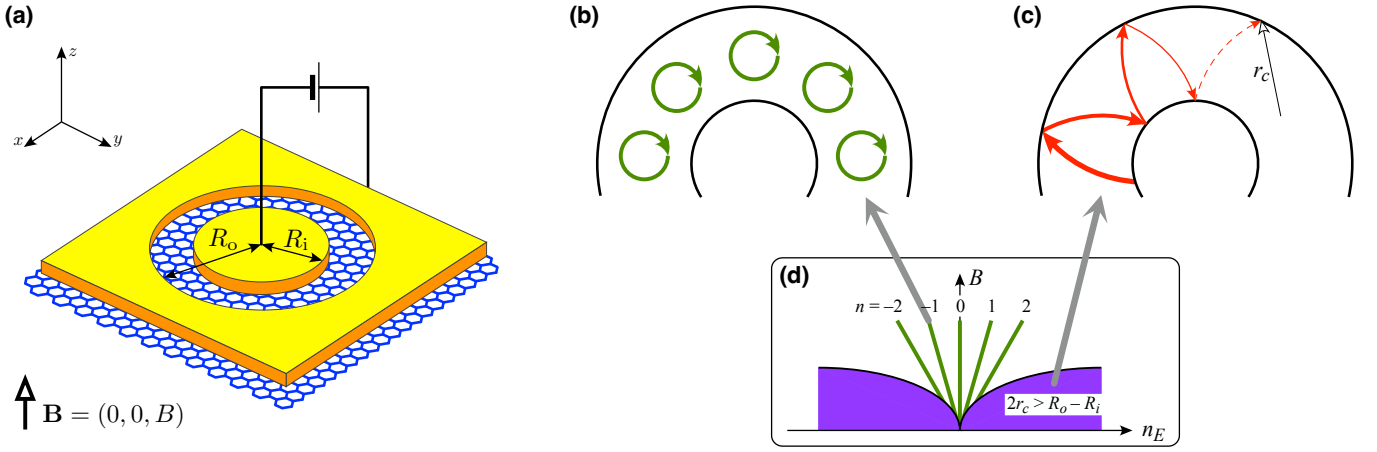


Figure 1: (a) The Corbino setup in graphene. Voltage source passes the current between the circular leads (yellow areas) via disk-shaped sample with the inner radii R_i and the outer radii R_o . Uniform magnetic field $\mathbf{B} = (0, 0, B)$ is perpendicular to the sample. Additional gate electrode (not shown) tunes the doping in the disk area. (b)–(d) Transport regimes for different fields and carrier concentrations n_E . At high fields, if doping is adjusted to a Landau level ($E = E_{nLL}$, $n = 0, \pm 1, \dots$) resonance occurs (b). At low field but high doping (such that the cyclotron diameter $2r_c > R_o - R_i$), incoherent scattering along classical trajectory governs the transport (c).

on distance from the origin in polar coordinates (r, φ) and is given by

$$V(r) = -V_0 \times \begin{cases} \frac{2^m |r - R_{av}|^m}{|R_o - R_i|^m} & \text{if } |r - R_{av}| \leq \frac{R_o - R_i}{2}, \\ 1 & \text{if } |r - R_{av}| > \frac{R_o - R_i}{2}, \end{cases} \quad (3)$$

where we have defined $R_{av} = (R_i + R_o)/2$ with R_i and R_o being the inner and outer radii of the disk. We also note that the limit of $V_0 \rightarrow \infty$ and $m \rightarrow \infty$ restores the familiar rectangular barrier of an infinite height [18, 19].

Because of the symmetry, the wave function can be written in a form

$$\Psi_j(r, \varphi) = e^{i(j-1/2)\varphi} \begin{pmatrix} \chi_a \\ \chi_b e^{i\varphi} \end{pmatrix}, \quad (4)$$

where $j = \pm 1/2, \pm 3/2, \dots$ is the total angular-momentum quantum number. In the leads, $r < R_i$ or $r > R_o$, the electrostatic potential energy is constant, $V(r) = -V_0$. In the case of electron doping, $E > -V_0$, the spinors $(\chi_a, \chi_b)^T$ for the incoming (i.e., propagating from $r = 0$) and outgoing (i.e., propagating from $r = \infty$) waves are given, up to the normalization, by

$$\chi_j^{\text{in}} = \begin{pmatrix} H_{j-1/2}^{(2)}(kr) \\ iH_{j+1/2}^{(2)}(kr) \end{pmatrix}, \quad \chi_j^{\text{out}} = \begin{pmatrix} H_{j-1/2}^{(1)}(kr) \\ iH_{j+1/2}^{(1)}(kr) \end{pmatrix}, \quad (5)$$

where $H_\nu^{(1)}(\rho)$ [$H_\nu^{(2)}(\rho)$] is the Hankel function of the first [second] kind, $k = |E + V_0|/(\hbar v_F)$, and we have set $B = 0$ in the leads [50]. (The wavefunctions for $B \neq 0$ are given explicitly in Refs. [17, 19].) Full wavefunctions in the leads, for a given j , can be written as

$$\chi_j^{(i)} = \chi_j^{\text{in}} + r_j \chi_j^{\text{out}}, \quad r < R_i, \quad (6)$$

$$\chi_j^{(o)} = t_j \chi_j^{\text{in}}, \quad r > R_o, \quad (7)$$

with the reflection (and transmission) amplitudes r_j (and t_j).

For the disk area, $R_i < r < R_o$, we have $B \neq 0$ and the position-dependent $V(r)$. Eq. (2) brought us to the system of ordinary differential equations for spinor components

$$\chi_a' = \left(\frac{j - 1/2}{r} + \frac{eBr}{2\hbar} \right) \chi_a + i \frac{E - V(r)}{\hbar v_F} \chi_b, \quad (8)$$

$$\chi_b' = i \frac{E - V(r)}{\hbar v_F} \chi_a - \left(\frac{j + 1/2}{r} + \frac{eBr}{2\hbar} \right) \chi_b, \quad (9)$$

which has to be integrated numerically for all j -s. To reduce round-off errors that occur in finite-precision arithmetic due to exponentially growing (or decaying) spinor components, we have divided the interval $R_i \dots R_o$ into M equally wide parts, bounded by $R_i^{(l)} < r < R_o^{(l)}$, with $l = 0, 1, \dots, M - 1$, and

$$R_i^{(l)} = R_i + l \frac{R_o - R_i}{M}, \quad R_o^{(l)} = R_i^{(l+1)}. \quad (10)$$

The resulting wave function for the l -th interval then has the form

$$\chi_j^{(l)} = A_j^{(l)} \chi_j^{(l),I} + B_j^{(l)} \chi_j^{(l),II}, \quad (11)$$

where $\chi_j^{(l),I}$, $\chi_j^{(l),II}$ denote the two linearly independent solutions that we obtained numerically by solving Eqs. (8,9) with two different initial conditions, $\chi_j^{(l),I}|_{r=R_i^{(l)}} = (1, 0)^T$ and $\chi_j^{(l),II}|_{r=R_i^{(l)}} = (0, 1)^T$. $A_j^{(l)}$ and $B_j^{(l)}$ are arbitrary complex coefficients.

The matching conditions, namely

$$\chi_j^{(i)}(R_i) = \chi_j^{(0)}(R_i), \quad (12)$$

$$\chi_j^{(l)}(R_o^{(l)}) = \chi_j^{(l+1)}(R_i^{(l+1)}), \quad l = 0, \dots, M - 2, \quad (13)$$

$$\chi_j^{(M-1)}(R_o) = \chi_j^{(o)}(R_o), \quad (14)$$

the quantum Hall regime. Therefore, a procedure described in this subsection is applied directly in all the following numerical examples, with wave functions in the leads given by Eqs. (6,7) for $m < +\infty$ (smooth potential barriers). For $m \rightarrow \infty$ (rectangular barrier), both the finite and infinite doping in the leads are studied for comparison.

The numerical integration of Eqs. (8,9) was performed for each of $M = 20$ intervals using a standard fourth-order Runge-Kutta (RK4) algorithm. For $R_o = 2R_i = 1000$ nm and $B < 0.5$ T, a spatial step of 0.5 pm was sufficient to reduce the unitarity error down to $\max(|\epsilon_j|) < 10^{-8}$. The summation over the modes was stopped when $T_j < 10^{-7}$. The Dormand-Prince method [52] was also implemented; however, no significant differences in the transmission probabilities were found compared to RK4.

B. Thermoelectric characteristics

Within the Landauer-Büttiker formalism, the linear-response conductance [53, 54] and other thermoelectric properties [55, 56] can be calculated from the transmission-energy dependence

$$\mathcal{T}(E) = \sum_{j=-j_{\max}}^{j_{\max}} T_j(E), \quad (21)$$

where $j_{\max} = \lfloor KR_i \rfloor - \frac{1}{2}$ (for heavily-doped leads, $j_{\max} \rightarrow \infty$), via dimensionless integrals

$$L_n = (k_B T)^{-n} \int dE \mathcal{T}(E) \left(-\frac{\partial f_{\text{FD}}}{\partial E} \right) (E - \mu)^n, \quad (22)$$

with $f_{\text{FD}}(\mu, T, E) = 1 / [\exp((E - \mu)/k_B T) + 1]$ the Fermi-Dirac distribution function and the chemical potential μ . In particular,

$$G = \frac{g_s g_v e^2}{h} L_0 \quad (\text{the conductance}), \quad (23)$$

$$S = \frac{dU}{dT} \Big|_{I=0} = \frac{k_B L_1}{e L_0} \quad (\text{the Seebeck coefficient}), \quad (24)$$

$$\mathcal{L} = \frac{K_{\text{el}}}{T G} = \frac{k_B^2 (L_0 L_2 - L_1^2)}{e^2 L_0^2} \quad (\text{the Lorentz number}), \quad (25)$$

where $g_s = g_v = 2$ are spin and valley degeneracies, $dU/dT|_{I=0}$ is the voltage derivative with respect to the temperature difference between the leads at zero electric current, and K_{el} is the electronic part of the thermal conductance.

For zero temperature, Eq. (23) reduces to

$$G(T \rightarrow 0) = g_0 \mathcal{T}(E_F), \quad (26)$$

where we have defined the conductance quantum $g_0 = 4e^2/h$ and the Fermi energy $E_F (= \mu \text{ for } T = 0)$. In turn, the zero-temperature conductance provides a direct insight into the transmission-energy dependence.

For some specific $\mathcal{T}(E)$, integrals in Eqs. (24,25) can be calculated analytically. In particular, $\mathcal{T}(E) \approx \text{const}$ leads

to $S \approx 0$ and $\mathcal{L} \approx \mathcal{L}_0 = (\pi^2/3) k_B^2/e^2$, which defines the Wiedemann-Franz law for metals [57]. For gapless Dirac systems, the corresponding approximation is $\mathcal{T}(E) \approx \mathcal{C}|E|$, with a constant $\mathcal{C} > 0$, for which both S and \mathcal{L} can be expressed by the polylogarithm function of $\mu/k_B T$ [30], with a universal (\mathcal{C} -independent) maxima $S_{\max} \simeq 1.0023 k_B/e$ and $\mathcal{L}_{\max} \simeq 2.3721 \mathcal{L}_0$. The latter value was first reported in the context of d -wave systems [58], before being found again for Dirac materials [59–61].

In the presence of a transport gap, one can consider a simplified model for $\mathcal{T}(E)$, given by

$$\mathcal{T}_{\text{model}}(E) = \mathcal{A} \delta(E) + \mathcal{B} \delta(E - \Delta E), \quad (27)$$

where $\mathcal{A} > 0$, $\mathcal{B} > 0$ are the constants, and $\delta(x)$ is the Dirac delta function. Generalizing the derivations presented in Refs. [31] and [42] to the asymmetric case ($\mathcal{A} \neq \mathcal{B}$), one finds easily

$$\frac{S_{\max} - S_{\min}}{2} \simeq \frac{k_B}{e} \left[\sqrt{u(u-1)} - \ln(\sqrt{u} + \sqrt{u-1}) \right], \quad (28)$$

$$\mathcal{L}_{\max} \simeq \left(\frac{k_B}{e} \right)^2 u^2 = \left(\frac{\Delta E}{2eT} \right)^2, \quad (29)$$

where $u = \Delta E/(2k_B T)$ and the asymptotic equalities correspond to $u \gg 1$. The remaining symbols in Eq. (28) are the maximum (S_{\max}) and the minimum (S_{\min}) Seebeck coefficient in the interval of $0 < \mu < \Delta E$. Note that the right-hand sides in Eqs. (28) and (29) depend only on u and the fundamental constants.

In a case where more δ -shaped peaks appear in the transmission spectrum $\mathcal{T}(E)$, as might be expected for the quantum Hall regime, the approximations given by Eqs. (28) and (29) are also valid, provided that a gap is identified with the maximum interval between the peaks ($\Delta E = \Delta E_{\max}$). The monotonicity of the right-hand sides in Eqs. (28) and (29) guarantees that the resulting approximations, for $\Delta E = \Delta E_{\max}$, correspond to the global maxima of the relevant quantities (i.e., the thermopower amplitude and the Lorentz number) as functions of μ .

III. RESULTS AND DISCUSSION

A. Zero-temperature conductance

Before discussing the thermoelectric properties, we present zero-temperature conductance spectra, which are related to the transmission-energy dependence via Eq. (26), and thus represent the input data for the calculation of the Seebeck coefficient and the Lorentz number. For the rectangular barrier of infinite height, $m, V_0 \rightarrow \infty$ in Eq. (3), the spectra are particle-hole symmetric, and it is sufficient to consider $\mu \geq 0$.

In Figs. 2(a) and 2(b) we display the disk conductance as a function of $\mu = E_F$ for $T = 0$. Resonances via Landau levels, centered near energies very close to the corresponding values for bulk graphene,

$$E_{n\text{LL}} \approx E_{n\text{LL}}^{\text{bulk}} = \text{sgn}(n) v_F \sqrt{2|n|e\hbar B}, \quad (30)$$

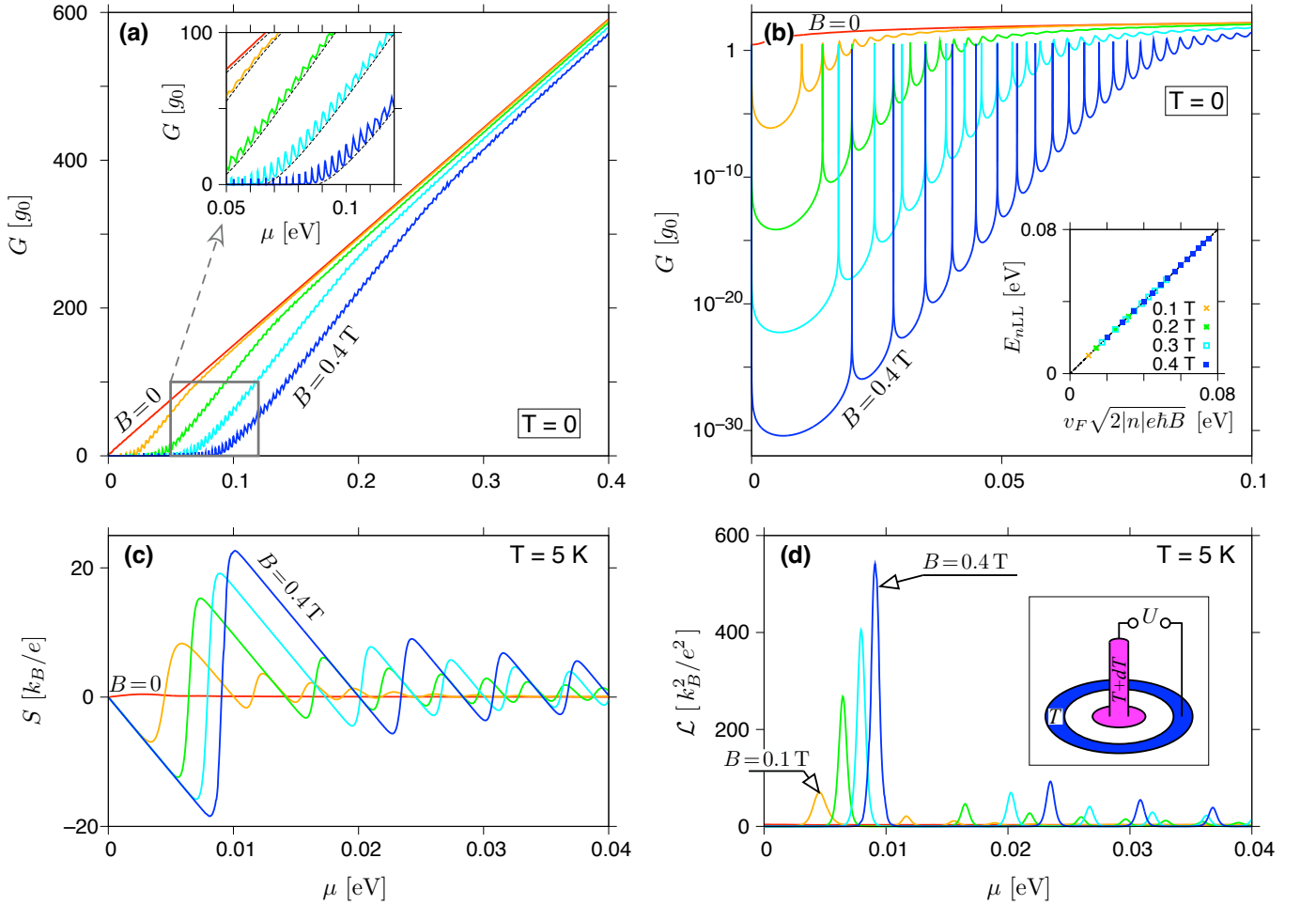


Figure 2: (a,b) Zero-temperature conductance, (c) the Seebeck coefficient and (d) the Lorentz number, both for $T = 5$ K, for the system of Fig. 1 with $R_o = 2R_i = 1000$ nm and the rectangular potential barrier [$V_0, m \rightarrow \infty$; see Eq. (3)] displayed as functions of the chemical potential. The magnetic field is varied from $B = 0$ (red solid lines in all plots) to $B = 0.4$ T (blue solid lines) with the steps of 0.1 T. Inset in (a) is a zoom-in, with black dashed lines depicting the incoherent conductance (see Appendix A). (b) shows same data as (a), but using the semilogarithmic scale, with the inset presenting positions of the actual transmission maxima for $B > 0$ (E_{nLL}) versus the values for bulk graphene [see Eq. (30)]. A setup for thermoelectric measurements is also depicted [see inset in (d)].

where n is an integer (without loss of generality, we hereinafter suppose $B > 0$), are clearly visible starting from a moderate value of $B = 0.1$ T. More generally, one can expect the resonances to be visible up to the n -th one if

$$E_{nLL} \lesssim E_{c,1} = \frac{v_F e B}{2} (R_o - R_i), \quad (31)$$

where $E_{c,1}$ denotes the threshold energy, below which the cyclotron diameter $2r_c = 2|E_F|/(v_F e B) < R_o - R_i$ and the incoherent transmission vanishes (see Appendix A). For instance, for $R_o = 2R_i = 1000$ nm discussed throughout the paper, Eq. (31) gives

$$|n| \lesssim 47.47 \times B [\text{T}], \quad (32)$$

coinciding with the number of well-separated maxima visualized in semi-logarithmic scale in Fig. 2(b).

It is also visible, for $|E_F| > E_{c,1}$, that the actual G grows rapidly with increasing $|E_F|$, closely following the prediction

for incoherent transport [see Fig. 2(a) and the inset]. This observation leads to the question whether E_{1LL} , or rather $2E_{c,1}$, defines the relevant transport gap to be substituted into Eqs. (28) and (29)?

This problem is solved via the numerical analysis of S and \mathcal{L} which will be presented next.

B. Thermopower and the Lorentz number

The Seebeck coefficient and the Lorentz number, calculated from Eqs. (24) and (25) for $T = 5$ K, are shown in Figs. 2(c) and 2(d) as functions of the chemical potential. Again, the particle-hole symmetry of $\mathcal{T}(E)$ guarantees that $S(\mu)$ is odd and $\mathcal{L}(\mu)$ is even on $\mu \rightarrow -\mu$, and it is sufficient to consider $\mu \geq 0$.

In the quantum Hall regime, i.e., for $|\mu| < E_{c,1}$, see Eq. (31), the $\mathcal{T}(E)$ function consists of narrow peaks, each cen-

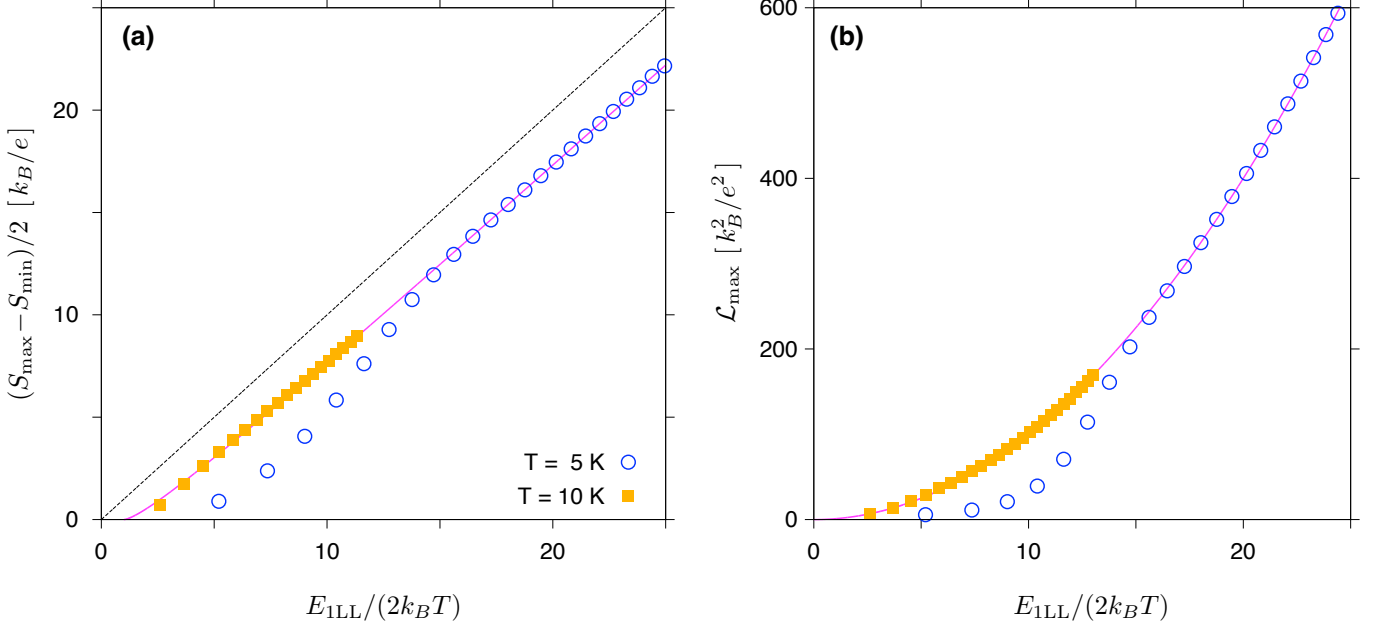


Figure 3: (a) Maximum amplitude of the Seebeck coefficient and (b) maximum Lorentz number for same system as in Fig. 2 at $T = 5$ K (open symbols) and $T = 10$ K (closed symbols) as functions of the maximum interval between Landau levels of $\Delta E_{\max} \equiv E_{1LL} = |E_{0LL} - E_{\pm 1LL}|$. Solid lines depict the asymptotic expressions given in Eqs. (28) and (29). Dashed line in (a) corresponds to the Goldsmid-Sharp relation, see Eq. (1), with $E_g = E_{1LL}$.

tered at E_{nLL} (see previous subsection). In such a case, reliable numerical estimations of the integrals L_0 , L_1 , and L_2 [see Eq. (22)] requires sufficiently dense sampling of $\mathcal{T}(E)$ near $E \approx E_{nLL}$.

The analytic structure of Eqs. (24) and (25) results in the following features visible in Figs. 2(c) and 2(d): First, each of the consecutive intervals, i.e., $E_{0LL} < E < E_{1LL}$, $E_{1LL} < E < E_{2LL}$, etc., contains a local minimum and a local maximum of S , surrounding an odd zero of S (even zeros occur for the resonances at $\mu \approx E_{nLL}$), which corresponds to a local maximum of \mathcal{L} . Second, the global extrema (corresponding to S_{\min} , S_{\max} , or \mathcal{L}_{\max}) are all in the first interval, $E_{0LL} < E < E_{1LL}$, characterized by the maximum width ($\Delta E_{\max} \equiv E_{1LL} - E_{0LL} = E_{1LL}$).

In Fig. 3 we plot the values of $(S_{\max} - S_{\min})/2$ and \mathcal{L}_{\max} against the dimensionless variable $E_{1LL}/(2k_B T)$, for the two values of $T = 5$ K and 10 K. Results of the numerical integration and subsequent optimization with respect to the chemical potential μ [datapoints] closely follow the approximations given in Eqs. (28,29) [solid lines], starting from $E_{1LL}/(2k_B T) \gtrsim 10$. The Goldsmid-Sharp formula [dashed line] produces a noticeable offset when compared to the Landauer-Büttiker results, but can still be used as a less accurate approximation for $(S_{\max} - S_{\min})/2$ for large $E_{1LL}/(2k_B T)$.

These results support our conjecture that the model $\mathcal{T}(E)$, given by Eq. (27), is able to reproduce the basic thermoelectric properties of graphene disk in the quantum Hall regime. Although it may seem surprising, at least at first glance, that the model $\mathcal{T}(E)$ with $\Delta E = E_{1LL}$ reproduces the actual numerical results, whereas the energy scale of $2E_{c,1} \gg E_{1LL}$ [see

Eq. (31)] seems to be irrelevant. However, for thermal excitation energies $k_B T \ll E_{1LL} \ll 2E_{c,1}$, the detailed behavior of the actual $\mathcal{T}(E)$ [see Eq. (21)] for $E - E_{0LL} = E \lesssim -k_B T$ or $E - E_{1LL} \gtrsim k_B T$ does not affect the integrals L_0 , L_1 , L_2 (note that the full width at half maximum for $-\partial f_{FD}/\partial E$ in Eq. (22) is $\approx 3.53 k_B T$) when $0 < \mu < E_{1LL}$). For this reason, a model with $\Delta E = E_{1LL}$ captures the essential features of the actual $\mathcal{T}(E)$, while focussing on the thermoelectric properties considered here.

C. Smooth potential barriers

For the sake of completeness, in this section we also revisit the effects of smooth potential barriers, considered earlier for zero magnetic field [49]. The electrostatic potential energy is given by Eq. (3), where the barrier height is fixed at $V_0 = t_0/2 = 1.35$ eV (for selected profiles for $m = 2, 8$, and ∞ , see Fig. 4) and the radii $R_o = 2R_i = 1000$ nm again.

For a finite barrier height, the particle-hole symmetry of the conductance spectrum $G(E)$ is absent, even for the rectangular barrier ($m = \infty$). However, for sufficiently low energies $|E| \ll V_0$ and large m , the Fermi wavelength $\lambda_F = \hbar v_F/|E|$ becomes longer than a characteristic length scale of a potential jump, i.e., $\Delta r = (L - L_{\text{eff}})/2$ where the sample length is $L = R_o - R_i = 500$ nm, and

$$L_{\text{eff}}^{(m)} = L \left(\frac{\hbar v_F}{LV_0} \right)^{1/m} \quad (33)$$

is the so-called diffusive length defined via $V(R_{\text{av}} \pm L_{\text{eff}}/2) = -\hbar v_F/L$ (see Ref. [48]). The value of $\hbar v_F/L$ can

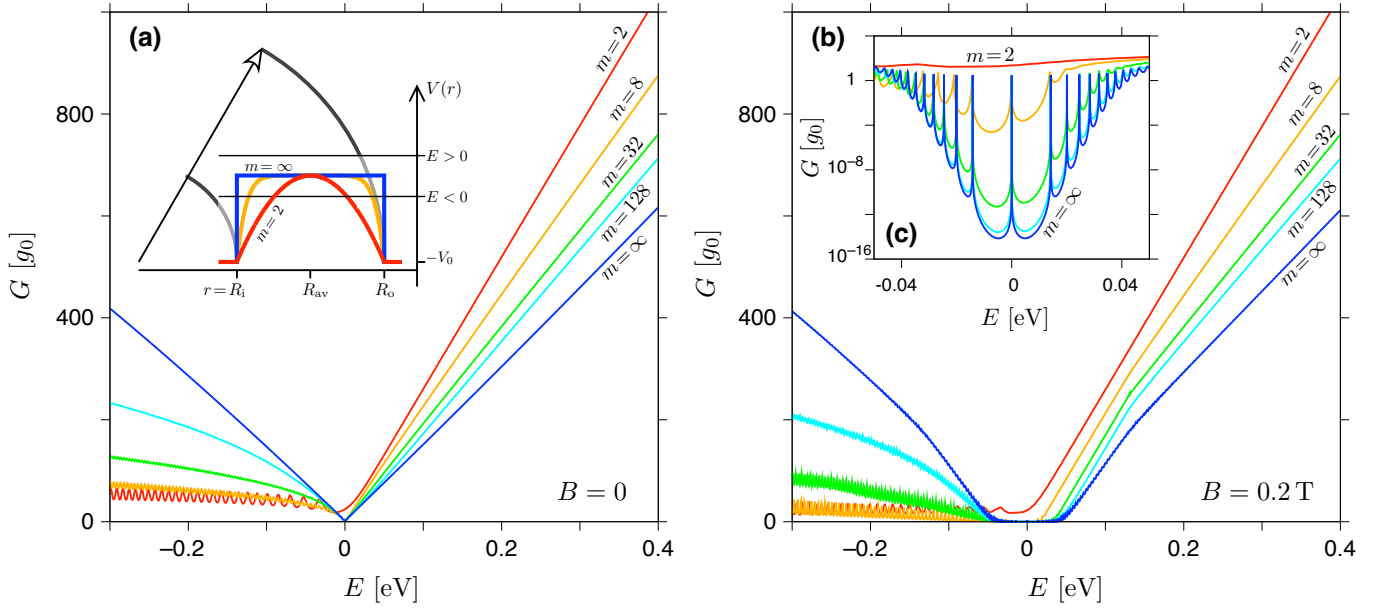


Figure 4: Zero-temperature conductance at (a) $B = 0$ and (b) $B = 0.2$ T versus the Fermi energy. The disk radii are same as Fig. 2, the barrier height [see Eq. (3)] is fixed at $V_0 = t_0/2 = 1.35$ eV, the parameter m is specified for each line. Inset in (a) shows selected potential profiles. (c) Zoom-in, for low energies, with same datasets as in (b) displayed in semi-logarithmic scale.

be attributed to the energy uncertainty corresponding to a typical time of flight $\sim L/v_F$ (up to the order of magnitude). We further note that $L_{\text{eff}}^{(m)} \rightarrow L$ for $m \rightarrow \infty$. If $\lambda_F \gg \Delta r$, the potential profile can be considered as approximately flat, and the approximate symmetry upon $E \rightarrow -E$ can be observed for the corresponding zero-field spectra shown in Fig. 4(a).

For $B = 0.2$ T, see Figs. 4(b) and 4(c), the approximate symmetry is also visible. In addition, it is worth noting that for $\lambda_F \gg \Delta r$ the lowest LLs are well pronounced, and their positions are almost unaffected compared to the infinite-barrier case [see previous subsection, Fig. 2(b)].

In both cases, i.e., for $B = 0$ and $B = 0.2$ T, the presence of two circular p-n junctions for $E < 0$ leads to a suppressed conductance compared to $E > 0$, with well-pronounced conductance oscillations due to quasi-bounded states (especially for smaller m). Due to such an asymmetry, the global conductance minimum G_{min} in the quantum Hall regime is typically reached in the energy interval of $-E_{1\text{LL}} < E < 0$, with the exception of the parabolic profile ($m = 2$), for which resonances with LLs are obliterated.

The consequences of the above-mentioned features of $G(E)$ for thermoelectric properties are discussed next.

In Fig. 5 we show pairs of plots analogous to those shown in Fig. 3, i.e., the thermopower amplitude $\Delta S = (S_{\text{max}} - S_{\text{min}})/2$, and the maximum Lorentz number \mathcal{L}_{max} , both displayed as functions of the dimensionless quantity $E_{1\text{LL}}/(2k_B T)$. This time, a step height is finite and four values of the exponent m (specified for each panel) are chosen. For sufficiently large $E_{1\text{LL}}/(2k_B T)$, the approximations of Eqs. (28) and (29) [solid lines] are closely followed by the actual datapoints also for smooth potentials ($m < +\infty$); we further note that the agreement is generally better for $T = 5$ K

[solid symbols] than for $T = 10$ K [open symbols].

The effect of $L_{\text{eff}}/L < 1$ corresponding to $m < +\infty$, see Eq. (33), and quantifying the potential smoothness, is further illustrated in Fig. 6, where we show selected thermoelectric properties, G_{min} , ΔS , and \mathcal{L}_{max} , as functions of L_{eff}/L . Each dataset corresponds to a fixed magnetic field ($B = 0.1$ T, 0.2 T, or 0.4 T), while the exponent m is varied from $m = 2$ to 512 , with an additional datapoint for rectangular barrier ($m = \infty$) placed at $L_{\text{eff}}/L = 1$. For finite-temperature characteristics, ΔS and \mathcal{L}_{max} , we set $T = 5$ K for $B = 0.1$ T; otherwise, T is chosen to keep the constant $E_{1\text{LL}}/(2k_B T)$ ratio (a quantity determining the approximate values ΔS and \mathcal{L}_{max} via Eqs. (28,29)).

Remarkably, the datasets for different B reveal some common behavior upon a proper rescaling; see three insets in Figs. 6(a), 6(b), and 6(c). In the first plot, it is easy to see that the conductance away from the resonances with LLs behaves approximately as $G_{\text{min}} \propto \exp(-\frac{1}{2}L_{\text{eff}}^2/l_B^2)$. In the next two plots, the datasets for the finite-temperature characteristics (ΔS and \mathcal{L}_{max}) come much closer to each other if plotted as functions of L_{eff}/l_B (where $l_B = \sqrt{\hbar/eB} \simeq 25.656 \text{ nm} \times (B [\text{T}])^{-1/2}$ is the magnetic length) than if simply plotted as functions of L_{eff} .

In addition, the behavior of G_{min} further validates the numerical stability of the approach presented in Sec. II. Namely, the value of $G_{\text{min}}/g_0 \sim 10^{-30}$ corresponds to the transmission amplitude $|t_j| \sim 10^{-15}$, which coincides with a typical round-off error in double precision arithmetic. This is also a reason why we have limited our discussion to $B \leq 0.4$ T (or, equivalently, $L/l_B \leq 12.33$ for $L = 500$ nm). For higher B , one must use numerical tools employing multiple precision [62]. In such a case, a significant slowdown of the computations can be expected.

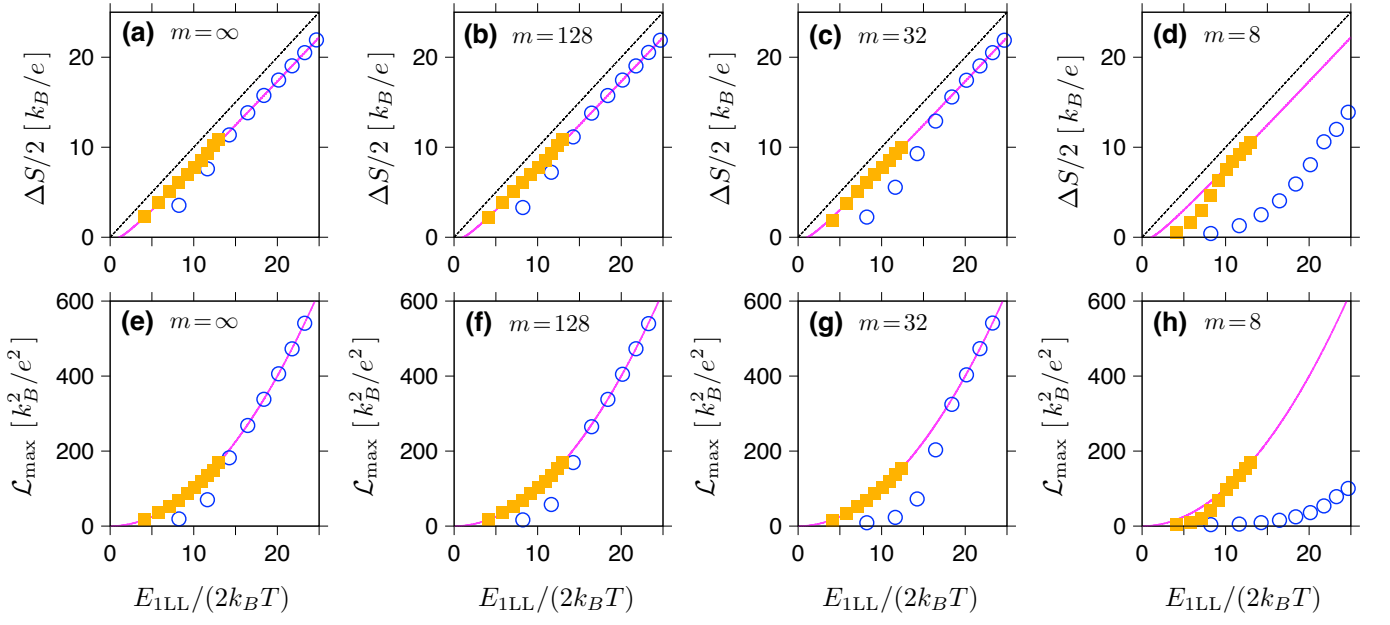


Figure 5: (a)–(d) Maximum amplitude of the Seebeck coefficient $\Delta S = (S_{\max} - S_{\min})/2$ and (e)–(h) maximum Lorentz number for same system as in Fig. 4 and selected values of the exponent m defining the potential profile [see Eq. (3)] displayed as the bulk Landau-level energy E_{1LL} obtained from Eq. (30) with $n = 1$. The line/color encoding is same as in Fig. 3.

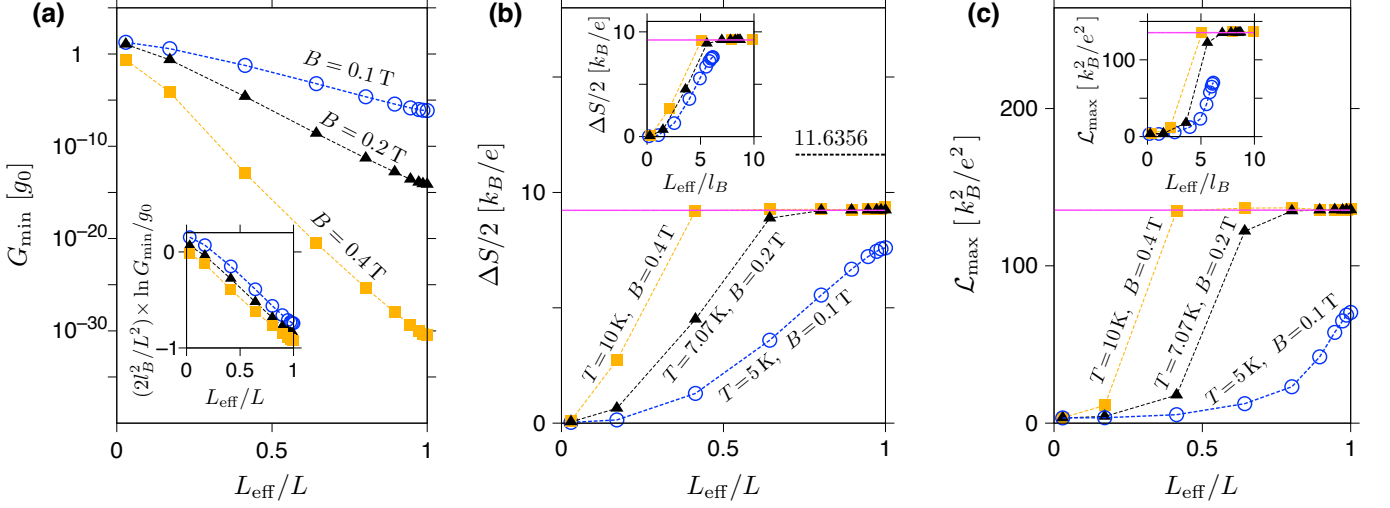


Figure 6: (a)–(c) Thermoelectric characteristics of the disk with smooth potential barriers in the quantum Hall regime displayed versus L_{eff} given by Eq. (33). (a) The minimum zero-temperature conductance reached for $-E_{1LL} < E < 0$, with inset visualizing the scaling according to $G_{\min} \propto \exp(-\frac{1}{2}L_{\text{eff}}^2/l_B^2)$ with $l_B = \sqrt{\hbar/eB}$ the magnetic length. (b) The maximum thermopower amplitude. (c) The maximum Lorentz number. Insets in (b,c) show same data as functions of the rescaled length L_{eff}/l_B . The magnetic field is varied between the datasets (see datapoints, dashed lines are guide for the eye only). Additionally, in (b,c) the temperature is varied to keep the constant $E_{1LL}/(2k_B T) \simeq 11.6356$. Solid horizontal lines in (b,c) mark the values following from Eqs. (28) and (29).

From a physical point of view, the considered values of B lead to the Zeeman splitting of $\Delta E_Z = g\mu_B B \approx 1.16 \cdot 10^{-4} \text{ eV} \times B [\text{T}] \ll E_{1LL}$, with $g \simeq 2$ and $\mu_B = e\hbar/(2m_e)$ the Bohr magneton. Throughout this paper the Zeeman term is therefore neglected.

IV. CONCLUSIONS

We have investigated selected thermoelectric properties of graphene-based Corbino disks in the presence of an external magnetic field. An efficient numerical scheme that allows the determination of these properties through mode matching for the Dirac equation, up to the magnetic fields that drive the system into the quantum Hall regime, using only a standard

double precision arithmetic, is put forward.

Our results show that both the thermopower amplitude and the maximal Lorentz number are determined by the energy interval separating the $n = 0$ and $n = \pm 1$ Landau levels (LLs) divided by the absolute temperature, and the fundamental constants. (The ratio of the disk radii, as well as the detailed shape of the electrostatic potential profile, are irrelevant.) Approximate expressions for the two above-mentioned thermoelectric characteristics can be derived by assuming the transmission-energy dependence to be in the form of two Dirac-delta peaks, centered at the energies of $n = 0$ and $n = 1$ (or $n = -1$) LLs. In particular, the expression describing the thermopower amplitude can be regarded as a modified version of the well-known Goldsmid-Sharp relation for semiconductors. It appears that a disk-shaped graphene sample, coupled to the two reservoirs in local thermal equilibrium, can act as a thermometer measuring the small temperature difference between the reservoirs (provided that applied field and average temperature are known).

Our analysis is carried out within the Landauer-Büttiker formalism for noninteracting quasiparticles. This implies that the fractional quantum Hall effect (FQHE) is outside the scope of this work. Although transmission resonances with FQHE states have been observed in ultraclean graphene samples [22], existing thermoelectric measurements for GaAs/AlGaAs disks [45, 47] indicate the presence of integer QHE states only. For this reason, a theoretical study of the thermoelectric signatures of integer QHE states had to be completed as a first step. Undoubtedly, generalizing the approach to include FQHE states would be a promising direction for future studies.

Acknowledgments

Main part of the work was supported by the National Science Centre of Poland (NCN) via Grant No. 2014/14/E/ST3/00256 (SONATA BIS). Computations were performed using the PL-Grid infrastructure.

Author contributions

A.R. designed the algorithm, A.R. and P.W. developed the code and performed preliminary computations, K.R. organized the computations on the PL-Grid supercomputing infrastructure; all authors were involved in data analysis and manuscript preparation.

Appendix A: Incoherent transport at magnetic field

Incoherent conductance (G_{incoh}) is calculated below by adapting the method presented in Ref. [49] for the uniform

magnetic field case.

Due to the disk symmetry, the incident angles, θ_1 for the interface at $r = R_i$ and θ_2 for the interface at $r = R_o$ (see Fig. 7) remain constant (up to a sign) during multiple scattering between the two interfaces. In turn, for a multimode regime, summing in Eq. (26) can be approximated by averaging over the modes, leading to

$$G_{\text{incoh}} = 2g_0 k_F R_i \langle T_{12} \rangle, \quad (\text{A1})$$

where

$$\langle T_{12} \rangle = \frac{1}{2} \int_{u_c}^1 du_1 \frac{T_1 T_2}{T_1 + T_2 - T_1 T_2}, \quad (\text{A2})$$

with

$$T_j = \frac{2\sqrt{1-u_j^2}}{1+\sqrt{1-u_j^2}}, \quad j = 1, 2, \quad (\text{A3})$$

being the transmission probabilities for a potential step of infinite height. The parameter $u_1 = \sin \theta_1$ is further regarded as an independent variable. u_c in Eq. (A2) denotes the minimal value of u_1 above which the corresponding $u_2 = \sin \theta_2$ satisfies $|u_2| \leq 1$.

Assuming a constant electrostatic potential energy in the disk area, the trajectory between subsequent scatterings forms an arc, with the radii $r_c = |E|/(v_F e B)$ (the cyclotron radius for massless Dirac particle at a field $B > 0$), centered at the distance r_x from the origin. Solving the two triangles with a common edge r_x (dashed line) and the opposite vertices in two scattering points, one easily finds

$$r_x^2 = R_i^2 + r_c^2 + 2R_i r_c \sin \theta_1 \quad (\text{A4})$$

(for the triangle containing a scattering point at $r = R_i$), and

$$r_x^2 = R_o^2 + r_c^2 - 2R_o r_c \sin \theta_2 \quad (\text{A5})$$

(for the triangle containing a scattering point at $r = R_o$), leading to

$$u_2 = \sin \theta_2 = \frac{R_o^2 - R_i^2 - 2R_i r_c u_1}{2R_o r_c}. \quad (\text{A6})$$

Therefore, the value of u_c in Eq. (A2) is given by

$$u_c = \begin{cases} -1, & \text{if } r_c \geq \frac{R_i + R_o}{2} \\ \frac{R_o^2 - R_i^2}{2R_i r_c} - \frac{R_o}{R_i}, & \text{if } \frac{R_i + R_o}{2} > r_c \geq \frac{R_o - R_i}{2} \\ 1, & \text{if } r_c < \frac{R_o - R_i}{2} \end{cases}. \quad (\text{A7})$$

In a zero-field limit, we have $r_c \rightarrow \infty$, leading to $u_c = -1$ and $u_2 \rightarrow -(R_i/R_o)u_1$. In such a limit, the integral in Eq. (A2) can be calculated analytically, leading to

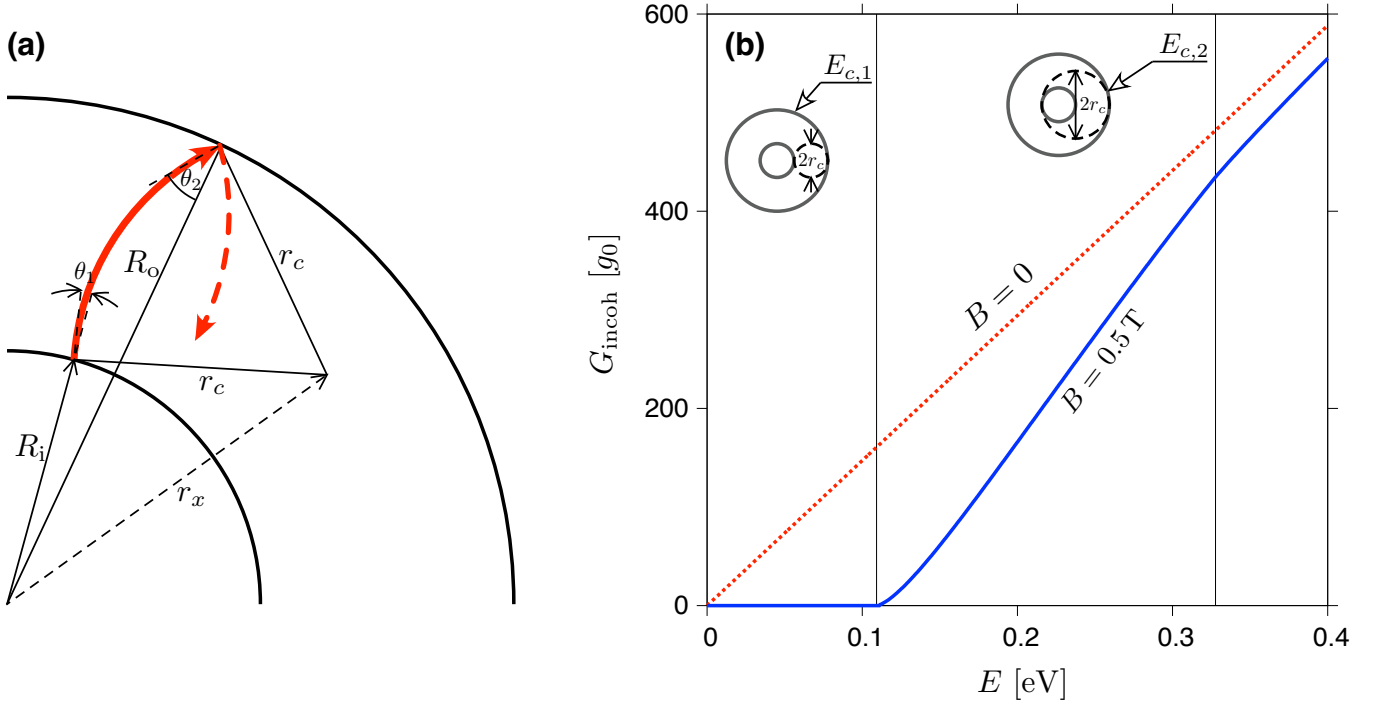


Figure 7: (a) Propagation between subsequent scatterings on interfaces at $r = R_i$ and $r = R_o$ (with incident angles θ_1, θ_2) in uniform magnetic field, defining the cyclotron orbit centered at $r = r_x$ with its radii r_c . (b) Incoherent conductance calculated from Eq. (A1) for $B = 0$ [dashed line] and $B = 0.5$ T [solid line]. The disk radii are $R_o = 2R_i = 1000$ nm; a rectangular potential barrier is considered. Characteristic Fermi energies $E_{c,1}$ and $E_{c,2}$ mark with vertical lines correspond to $r_c = (R_o - R_i)/2$ and $r_c = (R_i + R_o)/2$ (respectively).

$$G_{\text{incoh}}(B \rightarrow 0) = 2g_0 k_F R_i \frac{(2a + \frac{1}{a}) \arcsin a + 3\sqrt{1-a^2} - \frac{\pi}{2}(a^2 + 2)}{1-a^2}, \quad \text{with } a = R_i/R_o. \quad (\text{A8})$$

The above reproduces a zero-field result reported in Ref. [49]. For $B > 0$, the integration needs to be performed numerically.

From geometric point of view, the limiting values of r_c in Eq. (A7), i.e., $r_{c,1} = (R_o - R_i)/2$ and $r_{c,2} = (R_i + R_o)/2$, indicate three distinct situation: (i) none of the circular trajectories originating from $r = R_i$ can reach $r = R_o$ (the $r_c < r_{c,1}$ case), (ii) trajectories with some incident angles θ_1 may reach the second interface, but some cannot (the $r_{c,2} > r_c \geq r_{c,1}$ case), and (iii) all the trajectories originating from $r = R_i$ reach $r = R_o$ (the $r_c \geq r_{c,1}$ case).

Also in Fig. 7, we display G_{incoh} calculated numerically from Eq. (A1) for $B = 0$ and $B = 0.5$ T, with the remaining

system parameters same as considered throughout the paper. The Fermi energies $E_{c,\alpha} = v_F e B r_{c,\alpha}$, $\alpha = 1, 2$, for the $B = 0.5$ T case, are mark with vertical lines. It can be shown that for $E \approx E_{c,1}$, the incoherent conductance behaves as

$$G_{\text{incoh}}(E) \propto \Theta(E - E_{c,1}) |E - E_{c,1}|^{3/2}, \quad (\text{A9})$$

with $\Theta(x)$ being the Heaviside step function.

Remarkably (see the main text), G_{incoh} follows quite close the actual G calculated via the numerical mode matching, but thermoelectric characteristics are ruled by the Landau levels, with their energies being unrelated to the value of $E_{c,1}$.

- [1] K. S. Novoselov, A. K. Geim, S. V. Morozov, D. Jiang, Y. Zhang, S. V. Dubonos, I. V. Grigorieva, and A. A. Firsov, *Science* **306**, 666 (2004).
- [2] K. S. Novoselov, A. K. Geim, S. V. Morozov, D. Jiang, M. I. Katsnelson, I. V. Grigorieva, S. V. Dubonos, and A. A. Firsov, *Nature* **438**, 197 (2005).
- [3] Y. Zhang, Y.-W. Tan, H. L. Stormer, and P. Kim, *Nature* **438**,

201 (2005).

- [4] S. Das Sarma, S. Adam, E. H. Hwang, E. Rossi, *Rev. Mod. Phys.* **83**, 407 (2011).
- [5] A. V. Rozhkov, G. Giavaras, Y. P. Bliokh, V. Freilikher, and F. Nori, *Phys. Rep.* **503**, 77 (2011).
- [6] See, e.g.: M. I. Katsnelson, *The Physics of Graphene. Second Edition*, (Cambridge University Press, Cambridge, UK, 2020).

- DOI: <https://doi.org/10.1017/9781108617567>, Chapter 3.
- [7] G. H. Lee, D. K. Efetov, W. Jung, L. Ranzani, E. D. Walsh, T. A. Ohki, T. Taniguchi, K. Watanabe, P. Kim, D. Englund *et al.*, *Nature* **586**, 42 (2020).
- [8] T. Li, H. Da, X. Du, J. J. He, and X. Yan, *J. Phys. D: Appl. Phys.* **53**, 115108 (2020).
- [9] Y. Ronen, T. Werkmeister, D. H. Najafabadi, A. T. Pierce, L. E. Anderson, Y. J. Shin, S. Y. Lee, Y. H. Lee, B. Johnson, K. Watanabe *et al.*, *Nat. Nanotechnol.* **16**, 563 (2021).
- [10] A. Schmitt, P. Vallet, D. Mele, M. Rosticher, T. Taniguchi, K. Watanabe, E. Bocquillon, G. Fève, J. M. Berroir, C. Voisin *et al.*, *Nat. Phys.* **XX**, XXXX (2023).
- [11] C.-C. Kalmbach, J. Schurr, F. J. Ahlers, A. Müller, S. Novikov, N. Lebedeva, and A. Satrapinski, *Appl. Phys. Lett.* **105**, 073511 (2014).
- [12] F. Lafont, R. Ribeiro-Palau, D. Kazazis, A. Michon, O. Couturaud, C. Consejo, T. Chassagne, M. Zielinski, M. Portail, B. Jouault *et al.*, *Nat. Commun.* **6**, 6806 (2015).
- [13] M. Kruskopf and R. E. Elmquist, *Metrologia* **55**, R27 (2018).
- [14] M. Polini, F. Guinea, M. Lewenstein, H. C. Manoharan, and V. Pellegrini, *Nat. Nanotechnol.* **8**, 625 (2013).
- [15] M. Mattheakis, C. A. Valagiannopoulos, and E. Kaxiras *Phys. Rev. B* **94**, 201404(R) (2016).
- [16] D. J. Trainer, S. Srinivasan, B. L. Fisher, Y. Zhang, C. R. Pfeiffer, S.-W. Hla, P. Darancet, N. P. Guisinger, e-print: arXiv:2104.11334 (unpublished).
- [17] V. V. Cheianov and V. I. Fal'ko, *Phys. Rev. B* **74**, 041403(R) (2006).
- [18] A. Rycerz, P. Recher, and M. Wimmer, *Phys. Rev. B* **80**, 125417 (2009).
- [19] A. Rycerz, *Phys. Rev. B* **81**, 121404(R) (2010).
- [20] E. C. Peters, A. J. M. Giesbers, M. Burghard, and K. Kern, *Appl. Phys. Lett.* **104**, 203109 (2014).
- [21] B. Abdollahipour and E. Moomivand, *Physica E* **86** 204 (2017).
- [22] Y. Zeng, J. I. A. Li, S. A. Dietrich, O. M. Ghosh, K. Watanabe, T. Taniguchi, J. Hone, and C. R. Dean, *Phys. Rev. Lett.* **122**, 137701 (2019).
- [23] D. Suszalski, G. Rut, and A. Rycerz, *J. Phys. Mater.* **3**, 015006 (2020).
- [24] M. Kamada, V. Gall, J. Sarkar, M. Kumar, A. Laitinen, I. Gornyi, and P. Hakonen, *Phys. Rev. B* **104**, 115432 (2021).
- [25] Y. Yerin, V. P. Gusynin, S. G. Sharapov, and A. A. Varlamov, *Phys. Rev. B* **104**, 075415 (2021).
- [26] P. Dollfus, V. H. Nguyen, and J. Saint-Martin, *J. Phys.: Condens. Matter* **27**, 133204 (2015).
- [27] C. R. Wang, W.-S. Lu, L. Hao, W.-L. Lee, T.-K. Lee, F. Lin, I.-C. Cheng, and J.-Z. Chen, *Phys. Rev. Lett.* **107**, 186602 (2011).
- [28] Y. Y. Chien, H. Yuan, C. R. Wang, and W. L. Lee, *Sci. Rep.* **6**, 20402 (2016).
- [29] P. S. Mahapatra, K. Sarkar, H. R. Krishnamurthy, S. Mukerjee, and A. Ghosh, *Nano Lett.* **17**, 6822 (2017).
- [30] D. Suszalski, G. Rut, and A. Rycerz, *Phys. Rev. B* **97**, 125403 (2018).
- [31] D. Suszalski, G. Rut, and A. Rycerz, *J. Phys.: Condens. Matter* **31**, 415501 (2019).
- [32] P. Zong, J. Liang, P. Zhang, C. Wan, Y. Wang, and K. Koumoto, *ACS Appl. Energy Mater.* **3**, 2224 (2020).
- [33] Y. B. Dai, K. Luo, and X. F. Wang, *Sci. Rep.* **10**, 9105 (2020).
- [34] A. Jayaraman, K. Hsieh, B. Ghawri, P. S. Mahapatra, K. Watanabe, T. Taniguchi, and A. Ghosh, *Nano Lett.* **21**, 1221 (2021).
- [35] A. S. Ciepielewski, J. Tworzydło, T. Hyart, and A. Lau, *Phys. Rev. Research* **4**, 043145 (2022).
- [36] M.-J. Lee, J.-H. Ahn, J. H. Sung, H. Heo, S. G. Jeon, W. Lee, J. Y. Song, K.-H. Hong, B. Choi, S.-H. Lee, and M.-H. Jo, *Nature Commun.* **7**, 12011 (2016).
- [37] H. Sevinçli, *Nano Lett.* **17**, 2589 (2017).
- [38] D. Qin, P. Yan, G. Ding, X. Ge, H. Song, and G. Gao, *Sci. Rep.* **8**, 2764 (2018).
- [39] D. Li, Y. Gong, Y. Chen, J. Lin, Q. Khan, Y. Zhang, Y. Li, H. Zhang, and H. Xie, *Nano-Micro Lett.* **12**, 36 (2020).
- [40] L. Hao and T. K. Lee, *Phys. Rev. B* **81**, 165445 (2010).
- [41] H. J. Goldsmid and J. W. Sharp, *J. Electron. Mater.* **28**, 869 (1999).
- [42] A. Rycerz, *Materials* **14**, 2704 (2021).
- [43] S. Li, A. Levchenko, and A. V. Andreev, *Phys. Rev. B* **105**, 125302 (2022).
- [44] Y. Barlas and K. Yang, *Phys. Rev. B* **85**, 195107 (2012).
- [45] S. Kobayakawa, A. Endo, and Y. Iye, *J. Phys. Soc. Jpn.* **82**, 053702 (2013).
- [46] N. d'Ambrumenil and R. H. Morf, *Phys. Rev. Lett.* **111**, 136805 (2013).
- [47] M. Real, D. Gresta, C. Reichl, J. Weis, A. Tonina, P. Giudici, L. Arrachea, W. Wegscheider, and W. Dietsche, *Phys. Rev. Applied* **14**, 034019 (2020).
- [48] A. Rycerz and P. Witkowski, *Phys. Rev. B* **104**, 165413 (2021).
- [49] A. Rycerz and P. Witkowski, *Phys. Rev. B* **106**, 155428 (2022).
- [50] Numerical evaluation of the Hankel functions, $H_\nu(x)^{(1,2)} = J_\nu(x) \pm iY_\nu(x)$ with $\nu \geq 0$, are performed employing the double-precision regular [irregular] Bessel function of the fractional order $J_\nu(x)$ [$Y_\nu(x)$] as implemented in Gnu Scientific Library (GSL), see: <https://www.gnu.org/software/gsl/doc/html/specfunc.html#bessel-functions>. For $\nu < 0$, we use $H_{-\nu}^{(1)}(x) = e^{i\pi\nu} H_\nu^{(1)}(x)$ or $H_{-\nu}^{(2)}(x) = e^{-i\pi\nu} H_\nu^{(2)}(x)$.
- [51] E. Anderson, Z. Bai, C. Bischof, S. Blackford, J. Demmel, J. Dongarra *et al.*, *LAPACK Users' Guide*, Third Edition (Society for Industrial and Applied Mathematics, Philadelphia, USA, 1999).
- [52] J. R. Dormand, J.R. and P. J. Prince, *J. Comput. Appl. Math.* **6**, 19 (1980).
- [53] R. Landauer, *IBM J. Res. Dev.* **1**, 223 (1957).
- [54] M. Büttiker, Y. Imry, R. Landauer, and S. Pinhas, *Phys. Rev. B* **31**, 6207 (1985).
- [55] M. Paulsson and S. Datta, *Phys. Rev. B* **67**, 241403(R) (2003).
- [56] K. Esfarjani and M. Zebarjadi, *Phys. Rev. B* **73**, 085406 (2006).
- [57] C. Kittel, *Introduction to Solid State Physics*, 8th ed. (John Wiley and Sons, New York, NY, USA, 2005); Chapter 6.
- [58] S. G. Sharapov, V. P. Gusynin, and H. Beck, *Phys. Rev. B* **67**, 144509 (2003).
- [59] K. Saito, J. Nakamura, and A. Natori, *Phys. Rev. B* **76**, 115409 (2007).
- [60] H. Yoshino and K. Murata, *J. Phys. Soc. Jpn.* **84**, 024601 (2015).
- [61] M. Inglot A. Dyrdał, V. K. Dugaev, and J. Barnaś, *Phys. Rev. B* **91**, 115410 (2015).
- [62] See, e.g.: M. Nakata, *The MPACK (MBLAS/MLAPACK): A Multiple Precision Arithmetic Version of BLAS and LAPACK*, version 0.7.0 (2012); URL: <http://mplapack.sourceforge.net>.